ACS MATERIALS Au
AN OPEN ACCESS JOURNAL OF THE AMERICAN CHEMICAL SOCIETY

pubs.acs.org/materialsau Article

Synthesis and Structure Stabilization of Disordered Rock Salt Mn/V-Based Oxyfluorides as Cathode Materials for Li-Ion Batteries

Iris Blumenhofer, Yasaman Shirazi Moghadam, Abdel El Kharbachi,* Yang Hu, Kai Wang, and Maximilian Fichtner*

Cite This: https://doi.org/10.1021/acsmaterialsau.2c00064 Read Online

ACCESS | Metrics & More | Article Recommendations | Supporting Information

ABSTRACT: The demand for high-performance lithium-ion batteries and thus efficient cathode materials is steadily increasing. In addition to a high energy density and long lifetime, these should also be cost-effective and environmentally benign. Manganese-based materials have particular potential because manganese is available in sufficient quantities and can be supplied at a comparatively low cost. Hence, in this study, manganese-based disordered rock salt oxyfluorides $Li_2Mn_{1-x}V_xO_2F$ ($0 \leq x \leq 0.5$) are synthesized as cathode materials for lithium-ion batteries using high-energy mechanochemical ball-milling. The effect of partial vanadium substitution on the sample properties is analyzed, focusing on the electrochemical properties. Furthermore, a heat treatment process for stabilization of the samples is followed, where the morphology and structure of the samples are studied by powder X-ray diffraction and electron microscopy (SEM/TEM). The oxidation states of the transition metals in the synthesized compositions are further investigated using X-ray absorption near-edge structure spectroscopy. The data analysis reveals that the heat treatment resulted in increased symmetry and reduced defects of ball-milled compounds, but it may also affect the local fluorination degree in the structure. However, the results show that this treatment process has a beneficial effect on capacity retention of the formulated electrodes (~81% after 100 cycles), a faster response to the change of cycling rate, and less increase in charge-transfer resistance of the samples during cycling. Such a structural improvement attributed to mitigation of the surface/bulk defects is an additional input to the series of cathode candidates of low temperature stability.

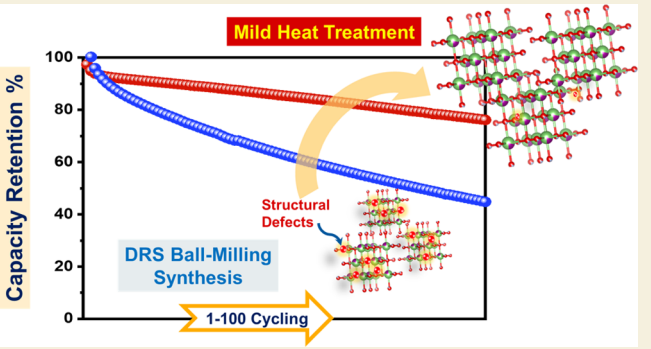

KEYWORDS: *Mn-based cathodes, disordered rock salt, oxyfluorides, structure stabilization, battery performance, X-ray absorption spectroscopy*

Downloaded via KIT BIBLIOTHEK on January 13, 2023 at 07:34:34 (UTC).
See https://pubs.acs.org/sharingguidelines for options on how to legitimately share published articles.

INTRODUCTION

The electrical properties and the performance of a battery cell, its lifetime, and safety rely directly on the chemical composition of the used electrode and electrolyte materials. One way to improve the performance features, for instance, the energy density of lithium-ion batteries (LIBs), is to choose a cathode material that can insert Li^+ with a high free energy difference to Li^0/Li^+, which is proportional to the cell voltage. In addition, the composition and structure of the cathode materials determine the specific capacity according to the number of lithium ions that can be reversibly inserted.[1−5] Up to now, several potential structures have been introduced to modify the widely used layered structure cathode materials with promising storage capacity and room for composition flexibility.[6] Among the alternatives, disordered rock salt (DRS) systems such as Li-rich transition-metal (TM) oxyfluorides show high potential.[7−10]

In order to use DRS materials as a cathode for LIBs, proper mobility of lithium ions through the material is required. This is possible if the lithium-to-TM ratio is sufficiently large to enable the formation of a percolation network within the structure with lithium excess.[11−13] Materials with the DRS structure exhibit a specific charge and discharge sloping profile.[14] They show a single-phase behavior in which lithium ions can be added or removed gradually.[15−17] This induces a constant change in the total energy of the system depending on how many lithium ions are packed into it.[2]

One critical issue with DRS cathode materials is that they generally tend to have undesirable rapid capacity fading.[9,10,18] Several causes are conceivable for this phenomenon,[19] such as undesirable reactions between the electrode material and the

Received: September 20, 2022
Revised: November 14, 2022
Accepted: December 5, 2022

© XXXX The Authors. Published by American Chemical Society

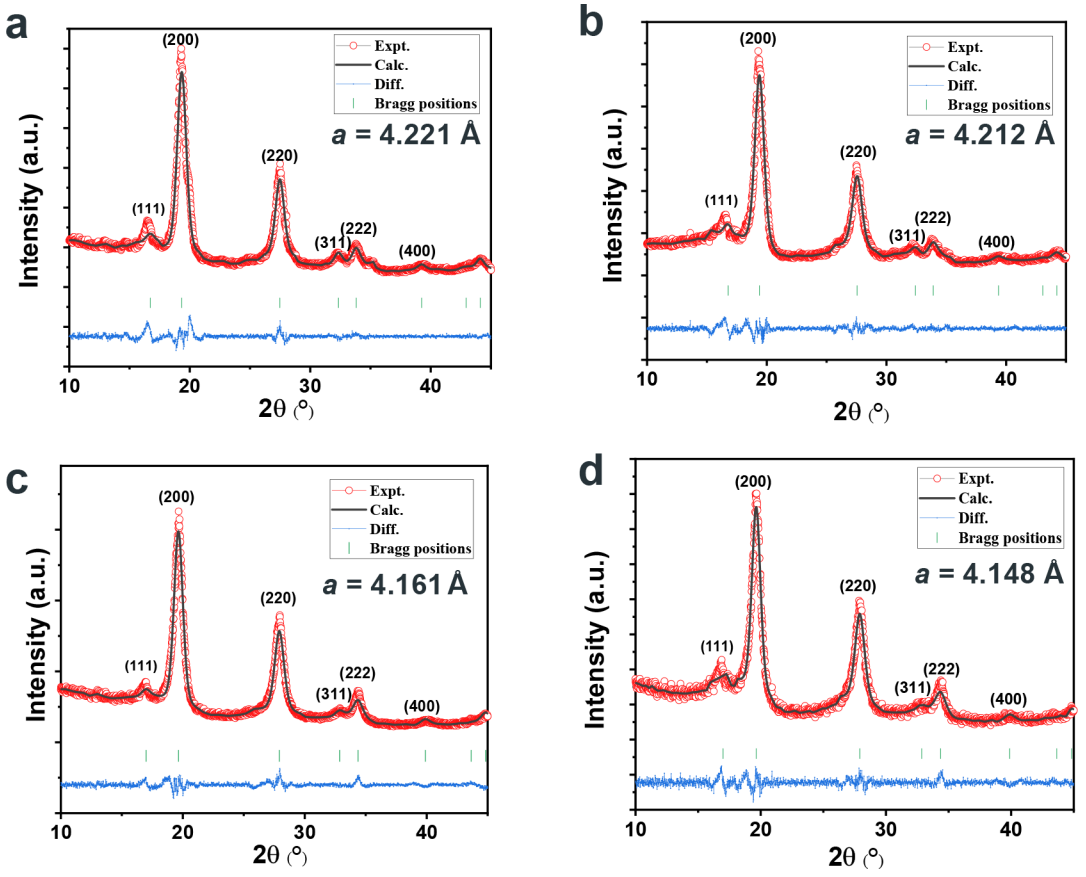

Figure 1. XRD patterns and results of Rietveld refinement of a DRS phase (*Fm*-3*m*) for (a) LMVOF, (b) HT-LMVOF, (c) LMOF, and (d) HT-LMOF.

electrolyte, which could lead to a drop in capacity and structural changes during cycling.[9,16] On the other hand, the dissolution of Mn from the cathode and subsequent migration to the anode, which is also observed in manganese-based spinels, could be an additional source of capacity fading.[9,20,21] Moreover, higher charging voltages can trigger oxygen redox reactions and/or carbon dioxide formation, resulting in irreversible O loss and further degradation.[18,22] To counteract capacity fading, the DRS oxyfluoride phase can be stabilized by replacing part of the initial TM with another as it can promote the formation of a structure at a lower Gibbs free energy.[7,10,23]

In the present study, we report the effects on the electrochemical performance of manganese being partially substituted by vanadium in a DRS material, emphasizing the beneficial contribution of heat treatment to structural stability. Two compounds were synthesized, Li_2MnO_2F (LMOF) and $Li_2Mn_{0.5}V_{0.5}O_2F$ (LMVOF), by mechanochemical ball-milling followed by further heat treatment. The structure, thermal stability, elemental distribution, and the chemical state of the samples have been systematically investigated using characterization tools (X-ray diffraction (XRD), differential scanning calorimetry (DSC), scanning electron microscopy/energy-dispersive X-ray spectroscopy (SEM/EDX), and X-ray absorption near-edge structure (XANES)). To assess the electrochemical properties and battery performance of the cathode composites, a series of electrochemical measurements was carried out to elucidate the redox and kinetic behaviors. In continuation, the electrochemical properties of the optimized electrodes are discussed and compared accordingly.

RESULTS AND DISCUSSION

Synthesis and Structural Characterization

Figure 1 shows the powder XRD patterns of the two synthesized materials LMOF and LMVOF. All the visible reflections can be indexed to a DRS structure. The substitution of only one-third of manganese by vanadium which should lead to the compound $Li_2Mn_{0.66}V_{0.33}O_2F$ was not successful since no pure DRS phase was formed, as can be seen from the XRD patterns in Figure S1a,b. This result is in agreement with the modeling prediction of the compositions with an activated Li percolation network in the pseudo-ternary system MnO-Li_2VO_3-LiF.[24] To ensure that the DRS structure is not altered by the heat treatment process, the temperature range was chosen based on the results of DSC measurements up to 400 °C (Figure S2). They show a wide thermal event, presumably due to the increase of the anisotropy in the crystal lattice, and a first-order phase transition, not completely reversible and taking place above 300 °C for both samples. The XRD result of the samples after DSC measurement at room temperature is shown in Figure S3. The patterns present some additional peaks which are not related to the DRS structure. This also suggests that the phase transition was only partially reversible. Therefore, a temperature of 300 °C was chosen as the upper limit for the heat treatment process.

As can be seen in Figures 1 and S1, the normal and the heat-treated (HT)-LMOF samples exhibit no significant presence of impurities, whereas the XRD pattern of both LMVOF samples indicates additional minor Bragg peaks of low intensity. A shoulder on the right side of the (200) reflection can be seen

https://doi.org/10.1021/acsmaterialsau.2c00064
ACS Mater. Au XXXX, XXX, XXX−XXX

in Figure S1c. This could be due to the presence of impurities, presumably of unreacted precursors. By comparing the XRD patterns of the synthesized material and the precursors, it is reasonable to assume that the impurity might be unreacted LiF. The LMVOF samples (normal and HT) show a visible shift to lower angles (2θ), which can be attributed to the partial substitution of manganese by vanadium. This substitution affects the structure of the DRS oxyfluoride, that is, its lattice parameters. Based on the pattern, it can be deduced that the LMVOF samples have larger lattice parameters. For both compositions, the HT samples show sharper peaks with a small shift to higher angles (2θ), indicating that the heat treatment process had an effect on the crystal structure of the samples. Figure 1 shows the Rietveld refinement analysis of all the samples. It can be seen that after heat treatment, the lattice parameter of both samples decreased, which is in agreement with the shift of the peak positions. Therefore, under a controlled atmosphere, it is observed that the powder sintering effect can be induced for the DRS oxyfluoride materials, as attested by the increased particle size/crystallite size (sharp XRD peaks), where the atomic diffusion across particle boundaries requiring activation energy is provided upon heating. The process is driven by lowering the internal energy of the system, mainly due to the reduction in the surface Gibbs free energy contribution and crystal rearrangement.

Figure S4 shows the SEM images of all four samples and the corresponding EDX chemical mapping. Based on the particle size and morphology analyses, the investigation indicates that there are some coarse particles of around 10 μm of different shapes but also many agglomerates of 200−500 nm. In general, the HT samples have slightly larger particles; however, the agglomerations are still present. The EDX results for all the samples show that all the elements are distributed homogeneously. Some traces of Fe in LMVOF samples have also been detected, probably originating from the stainless steel jar. To further understand the morphology, elemental distribution in the crystallites, and the crystal structure of the normal LMVOF sample, transmission electron microscopy (TEM), EDX, and selected area electron diffraction (SAED) analyses were performed. The morphology of the as-prepared sample characterized by the TEM (Figure 2a) showed that the particle size of the sample randomly differs from tens of nanometers to few micrometers. The corresponding SAED pattern in Figure 2b presented bright circular rings, which correspond to the (111), (200), (220), and (222) planes of a rock salt structure (*Fm*-3*m*), in good agreement with the analysis of XRD results in Figure 1. Also the EDX mapping results shown in Figure 2c presented a homogenous elemental distribution of the LMVOF sample.

To determine the oxidation state of manganese and vanadium in the synthesized composites, X-ray absorption spectroscopy was performed. Figure 3a shows the normalized Mn K-edge XANES spectra collected from LMOF and LMVOF, in comparison with various reference standards of known manganese oxidation states. From the Mn^0 metal to $Mn^{IV}O_2$, their absorption edges exhibited a progressive shift toward higher energy with an increasing oxidation state. Both LMOF samples (normal and HT) demonstrated an absorption edge close to that of $Mn^{III}{}_2O_3$, indicating an average oxidation state of 3+ for manganese. In contrast, a lower average oxidation state near $Mn^{II}O$ can be observed for the LMVOF samples. Consequently, in both cases, manganese maintains its oxidation state compared to the precursors used, and the heat treatment does not appear to have any effect on the oxidation states.

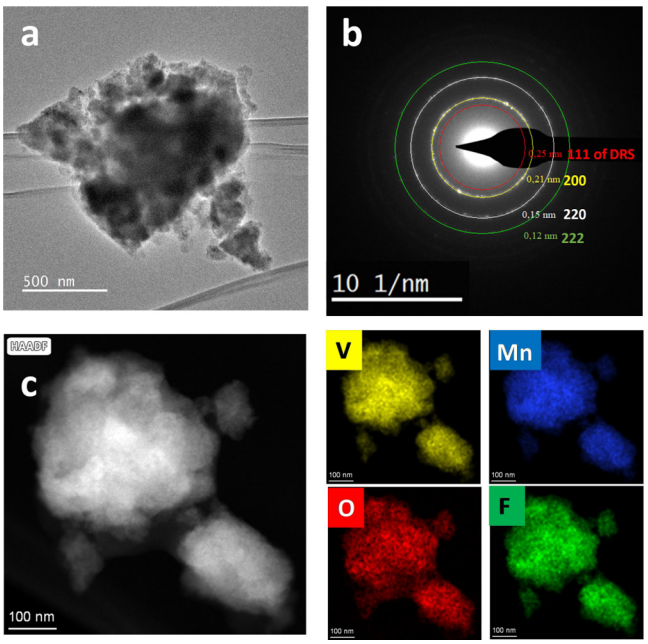

Figure 2. TEM image (a), SAED pattern (b), and high-angle annular dark-field scanning TEM (HAADF−STEM) image and EDX mapping of the LMVOF sample (c).

On the other hand, both LMVOF samples exhibited similar energy positions for the vanadium K-edge, which are between $V^{III}{}_2O_3$ and $V^{IV}O_2$, as seen in Figure 3b in which the inset highlights the pre-edge region. As the vanadium pre-edge is associated with the 1s → 3d transition, the distinguishable pre-edge features observed for both LMVOF samples evidenced a substantial distortion of the sixfold V−O (F) coordination in their DRS structure, which increased the p−d mixing of 3d states making the 1s → 3d transition no longer dipole-forbidden. The pre-edge peak intensity reflects the extent of deviation from centrosymmetry, so the weaker pre-edge in HT-LMVOF suggested that the heat treatment mitigated the local distortion. Pre-edge peak fitting was applied using a Gaussian peak model with a linear + Lorentzian baseline function, as shown in Figure 3c. The fitted pre-edge peak centroid for the oxide standards showed an increase with higher oxidation states of the vanadium central absorber, and both LMVOF demonstrated a pre-edge position close to $V^{III}{}_2O_3$ (Table 1), suggesting an average oxidation state of 3+. Therefore, from both the Mn and V K-edge spectra, it is observed that there is no charge-transfer occurring between TMs during the high-energy ball-milling process, and the synthesized compounds can be assumed to keep the oxidation state of the starting precursors.

Electrochemical Tests and Ex Situ Analysis

Galvanostatic cycling was performed for up to 100 cycles at a rate of 0.1 C (Figure 4) for LMOF- and LMVOF-based cathodes, both before and after the heat treatment process. The obtained charge and discharge sloping profiles of all samples confirm the single-phase behavior typical for DRS materials.[12,15,16] As depicted in Figure 4, the discharge capacity for all samples decreases with an increasing number of cycles.[9,10,17] The normal LMOF shows the largest difference

https://doi.org/10.1021/acsmaterialsau.2c00064
ACS Mater. Au XXXX, XXX, XXX−XXX

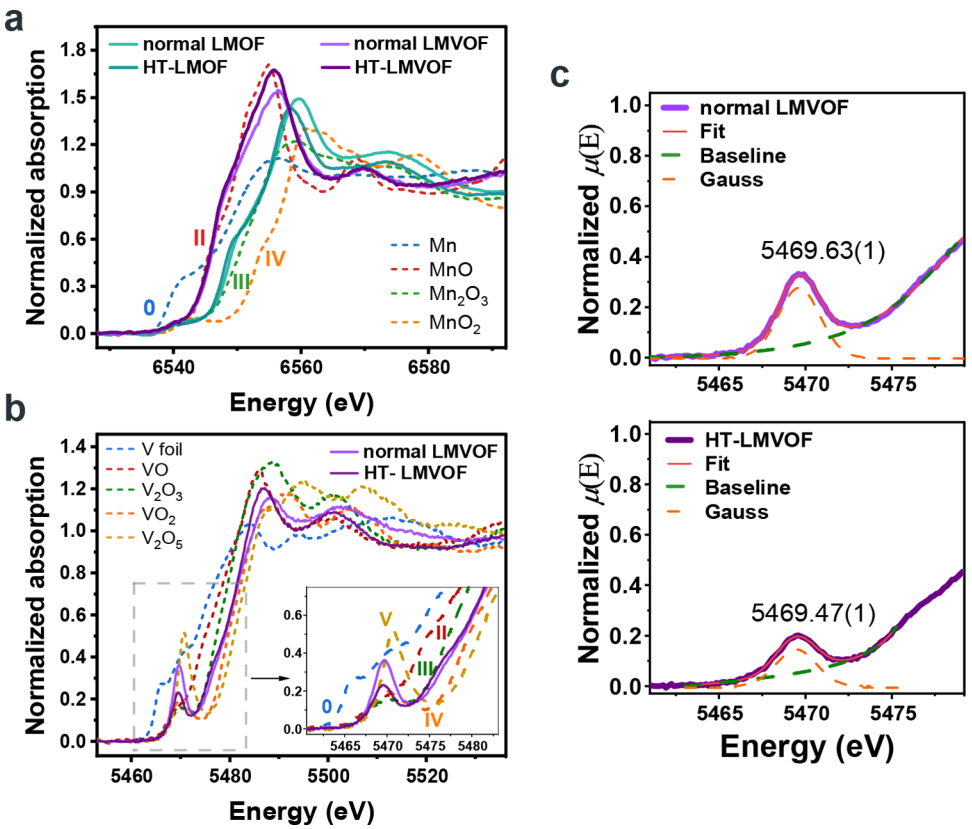

Figure 3. (a) Normalized Mn K-edge XANES spectra for LM(V)OF with standards and (b) normalized V K-edge XANES spectra for LMVOF with standards. The inset highlights the pre-edge region. (c) Examples of pre-edge fitting for LMVOF using a Gaussian peak model with a linear + Lorentzian baseline function, and the inset number indicates the fitting peak centroid. The same fitting procedure was applied to V_2O_3, VO_2, and V_2O_5.

Table 1. Pre-Edge Fitting Results for LMVOF and V Oxide Standards

compounds	pre-edge fitting using a Gaussian peak model with a linear + Lorentzian baseline function		
	peak centroid (eV)	amplitude	peak height
V_2O_3	5469.55 ± 0.05	0.57 ± 0.06	0.113 ± 0.007
VO_2	5470.10 ± 0.03	0.80 ± 0.03	0.176 ± 0.003
V_2O_5	5470.66 ± 0.02	1.33 ± 0.03	0.380 ± 0.005
normal LMVOF	5469.63 ± 0.01	0.83 ± 0.01	0.276 ± 0.002
HT-LMVOF	5469.47 ± 0.01	0.42 ± 0.01	0.145 ± 0.002

between the initial and final capacities (after 100 cycles). Interestingly, the HT-LMOF sample shows the smallest capacity decay upon cycling. On closer inspection and comparison of the curves of the two composites, it is noticeable that they differ in shape. The discharge curves of both LMOF samples for the 2nd, 10th, and 50th discharge cycles initially flatten out in the range from 4.3 V to about 2.8 V followed by a steep slope to 1.5 V. This hints at a change in the diffusion regime at the end of lithiation, which is not evident in the LMVOF samples. Note that during the discharge, the diffusion process would become energetically harder owing to the cubic close packed structure and limited diffusion channels, along with a change in the electronic conductivity with Li^+ insertion. This seems to affect the voltage profile with increased pure charge-transfer contribution. In addition, the LMOF-based cathodes show a higher capacity over a wider voltage range, which consequently leads to a higher energy content of the cell.

The normal LMOF shows an initial discharge capacity of 215 mAh g^{-1}, which is slightly higher than that of the normal LMVOF (213 mAh g^{-1}). LMOF also showed a better capacity retention (Figure 5) up to about the 80th cycle. However, between the 50th and 100th cycles, the capacity of LMOF decreases much more than that of LMVOF. Hence, the capacity retention after 100 cycles of the LMVOF sample is 12.4% higher for the LMVOF sample than for the LMOF sample (LMOF: 31.4% and LMVOF: 43.8%). It should be mentioned that the LMVOF sample showed a lower average voltage during cycling. This could also be proven by the cyclic voltammetry (CV) results (Figures S5 and S6).

The effect of heat treatment on galvanostatic cycling is shown in Figures 4c,d and 5b. After heat treatment, both materials exhibited a lower initial discharge capacity than the normal samples. This was somewhat higher for LMVOF (188 mAh g^{-1}) than for LMOF (178 mAh g^{-1}). However, the capacity of HT-LMOF after 100 cycles (144 mAh g^{-1}) was significantly higher than that of normal LMOF (68 mAh g^{-1}). In the case of HT-LMVOF, the discharge capacity was about 93 mAh g^{-1}, which corresponds to an increase in capacity retention to 49.6%. Consequently, HT-LMOF showed the highest capacity retention of 80.8% after 100 cycles. Furthermore, Figure 4 indicates that the average voltage of the HT-LMVOF sample has increased by around 0.1 V, whereas the average voltage of HT-LMOF stayed the same as the normal sample.

To determine the rate capability, the four samples were cycled within a voltage range of 1.5−4.3 V at 25 °C by varying

https://doi.org/10.1021/acsmaterialsau.2c00064
ACS Mater. Au XXXX, XXX, XXX−XXX

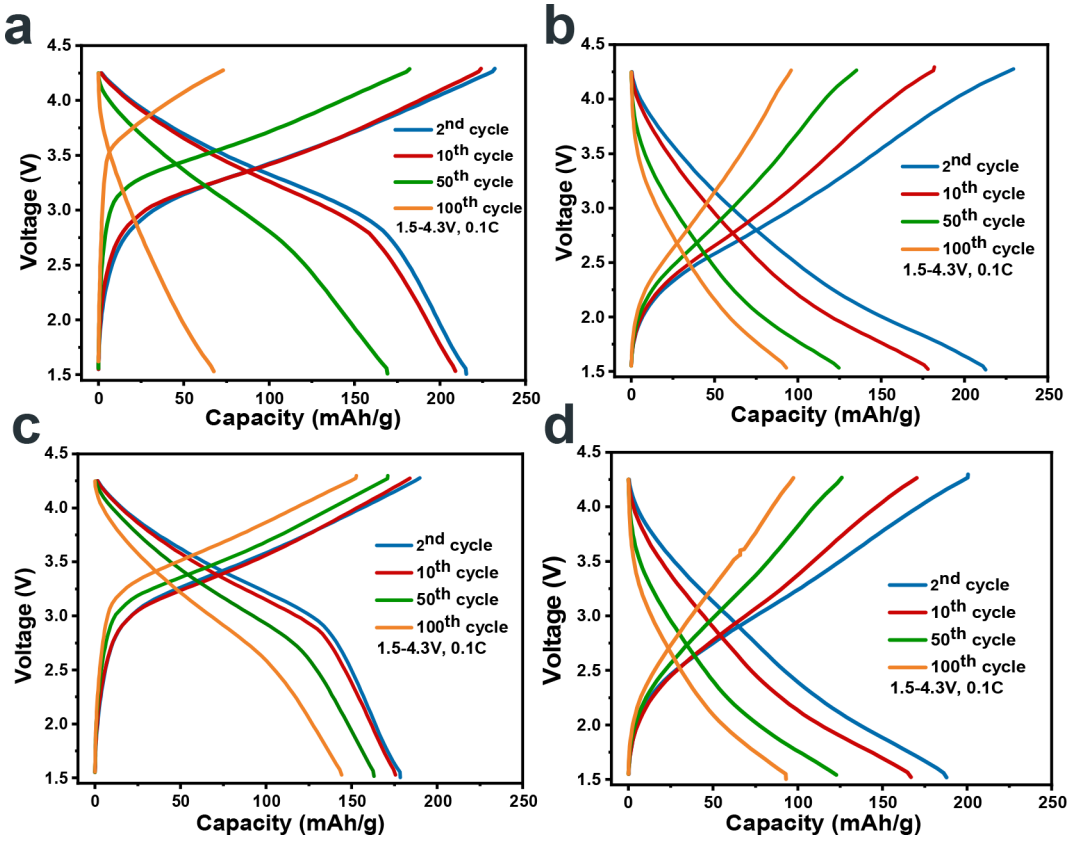

Figure 4. Galvanostatic charge and discharge profiles for the 2nd, 10th, 50th, and 100th cycles for (a) LMOF, (b) LMVOF, (c) HT-LMOF, and (d) HT-LMVOF (voltage range: 1.5−4.3 V, 0.1 C, and 25 °C).

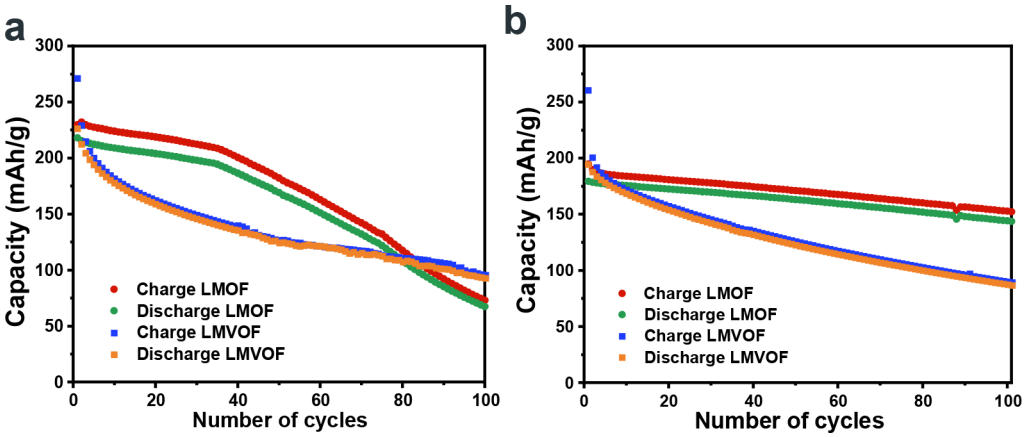

Figure 5. Capacity retention of (a) both normal LMOF- and LMVOF-based electrode materials and (b) both HT-LMOF- and HT-LMVOF-based electrode materials depending on the cycle number (1.5−4.3 V, 0.1 C, and 25 °C).

the current rate from 0.1 to 1 C. Figure 6a,b reveals that the LMOF electrodes exhibit a higher capacity at all rates and a better response to different rates. This deviation in response is particularly evident in the two normal samples. LMOF showed the smallest differences in capacity at different rates, whereas LMVOF exhibited the largest. By changing the cycling rate back to 0.1 C, the capacities indicated a little difference due to slight aging. This is the case for both the LMOF electrodes, including the normal LMVOF. However, HT-LMVOF shows quite a larger difference between the two 0.1 C rate sections mentioned. The Coulombic efficiency of both the LMVOF cathodes was higher than that of the LMOFs and close to 100%. The comparison of Figure 6a,b reveals that the Coulombic efficiency of LMOF is significantly increased by heat treatment. For LMVOF, the heat treatment causes an improvement in the rate capability.

To better understand the redox processes and determine the working potentials during the electrochemical cycling, CV measurements were performed for all samples at different rates (Figure S5), and the results of 0.1 mV/s rate are plotted in Figure S6. The curves of both LMOF samples (normal and HT) indicate a redox reaction at a voltage of about 3.3−3.4 V. Based on the XANES results presented above and comparable material ($Li_2Mn_xTi_{1-x}O_2F$),[7] this peak should be related to the

https://doi.org/10.1021/acsmaterialsau.2c00064
ACS Mater. Au XXXX, XXX, XXX−XXX

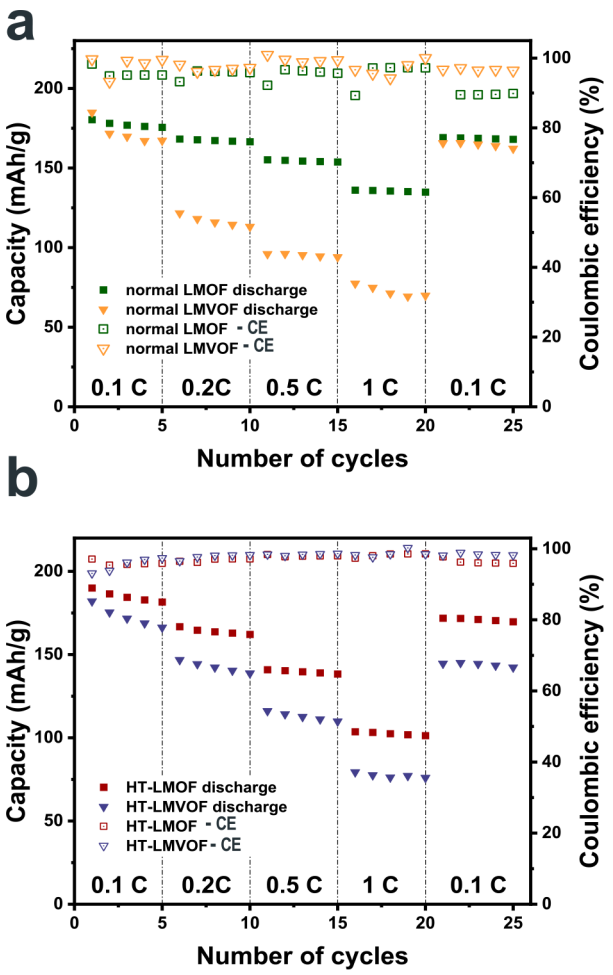

Figure 6. Rate capability of (a) normal LMOF and LMVOF electrode materials and (b) HT-LMOF and HT-LMVOF electrode materials by varying current rates from 0.1 C to 1 C (voltage range: 1.5−4.3 V). For clarity, the first activation cycle is omitted. CE: Coulombic efficiency.

oxidation of Mn^{3+} to Mn^{4+}. More than one maximum is visible in the CV results of the LMVOF samples, indicating that at least two redox processes are occurring.[25] Based on the oxidation state of manganese determined by XANES, the first redox peak at approximately 2.6 V could be related to the redox reaction of Mn^{2+}/Mn^{3+}. The second peak at around 3.2 V indicates the subsequent oxidation to Mn^{4+}.[7] It can be concluded that vanadium may be electrochemically inactive in this compound. However, the vanadium content can obviously affect the redox voltage of manganese and furthermore leads to a double redox reaction of manganese. After the heat treatment, both samples showed sharper CV peaks. This could be a sign of faster kinetics, which has already been demonstrated by the better rate capability of the HT samples.[25]

Figure 7 shows the Mn K-edge X-ray absorption fine structure (XAFS) spectra measured on LMOF from a synchrotron source. The normalized XANES spectra of pristine normal LMOF and the cycled electrodes (20 cycles) of normal and HT-LMOF showed an edge energy close to that of Mn_2O_3, as seen in Figure 7a. This indicates an average Mn^{3+} in the discharged/lithiated state, which is similar to the pristine LMOF (Figure 3) and a reversible manganese redox behavior for the first 20 cycles. A similar Fourier transform of extended XAFS (EXAFS) data confirmed almost identical local coordination in all cases as shown in Figure 7b, though both cycled electrodes exhibited a higher magnitude than the pristine material, which suggests reduced local disordering after cycling. A slightly higher Fourier transform peak magnitude was observed for the first and the second coordination shells in HT-LMOF_20C suggesting reduced local disordering probably induced by the heat treatment. Shell fitting was performed (Table 2) on the first Mn−O/F and the second Mn−Mn coordination shells. A higher Mn−O/F interatomic distance and a little increase of the Mn−Mn path length were obtained for HT-LMOF. It can be deduced that the heat treatment contributes to the increase of symmetry and mitigation of defects of ball-milled compounds, but it may also affect the local fluorination degree in the structure.

Figure 8 shows the V and Mn K-edge XANES spectra of the cycled HT-LMVOF electrode in the discharged state. The Mn K-edge shifted slightly toward higher energy, indicating a modest increase of the Mn oxidation state. On the other hand, the V K-edge demonstrated a prominent edge shift and a sharp pre-edge increase, suggesting that the average oxidation state of vanadium had been increased from 3+ to 4+. It seems that after prolonged cycling, both V and Mn were slightly oxidized, mainly the oxidation state of Mn, which could be affected by the Mn dissolution.

Electrochemical impedance spectra were collected for all four samples in the discharge state (1.5 V) for the initial cycle and after the 25th and 50th cycles, as shown in Figure 9. The resistance in the initial state of normal LMOF and LMVOF electrodes is comparable in magnitude. However, the resistance of the LMVOF cell increased faster upon cycling, which correlates to a faster degradation process for this sample.[26] After heat treatment, LMOF showed a higher resistance increase during cycling, whereas the electrode resistance of LMVOF decreased during cycling. It should be noted that multiple electrochemical impedance spectroscopy (EIS) scans of different samples showed reproducible results. Figure 10 shows the resistive components extracted by equivalent circuit (EC) fitting. For instance, the impedance results obtained from the normal LMOF after 25 cycles exhibited two partially overlapped semicircles in the medium-frequency range, representing two processes with distinct time constants. The higher-frequency contribution was considered to be due to a surface passivation layer ($R_s//Q_{sf}$) and the medium-frequency one to the charge-transfer ($R_{ct}//Q_{dl}$), followed by a mass transport-controlled process ($R_d//Q_d$) in the low-frequency region. However, the surface layer and charge-transfer processes were mostly undistinguishable and an overall electrode resistivity contribution from the summation of R_{sf} and R_{ct} was considered. As shown in Figure 10c, the heat treatment led to an increase in R_e at extended cycles for HT-LMOF but reduced the electrode resistance for HT-LMVOF upon cycling. The impedance of HT-LMOF (Figure S7b) after 50 full cycles showed a large resistance but indistinguishable time constants from medium to low frequencies. Therefore, it could not be fitted using the same EC model and so the results are not shown in Figure 10c.

CONCLUSIONS

In this study, we synthesized two DRS structures using mechanochemical ball-milling and investigated their structural and electrochemical properties. This includes the analysis of XRD patterns, XANES results, and SEM/EDX images as well

https://doi.org/10.1021/acsmaterialsau.2c00064
ACS Mater. Au XXXX, XXX, XXX−XXX

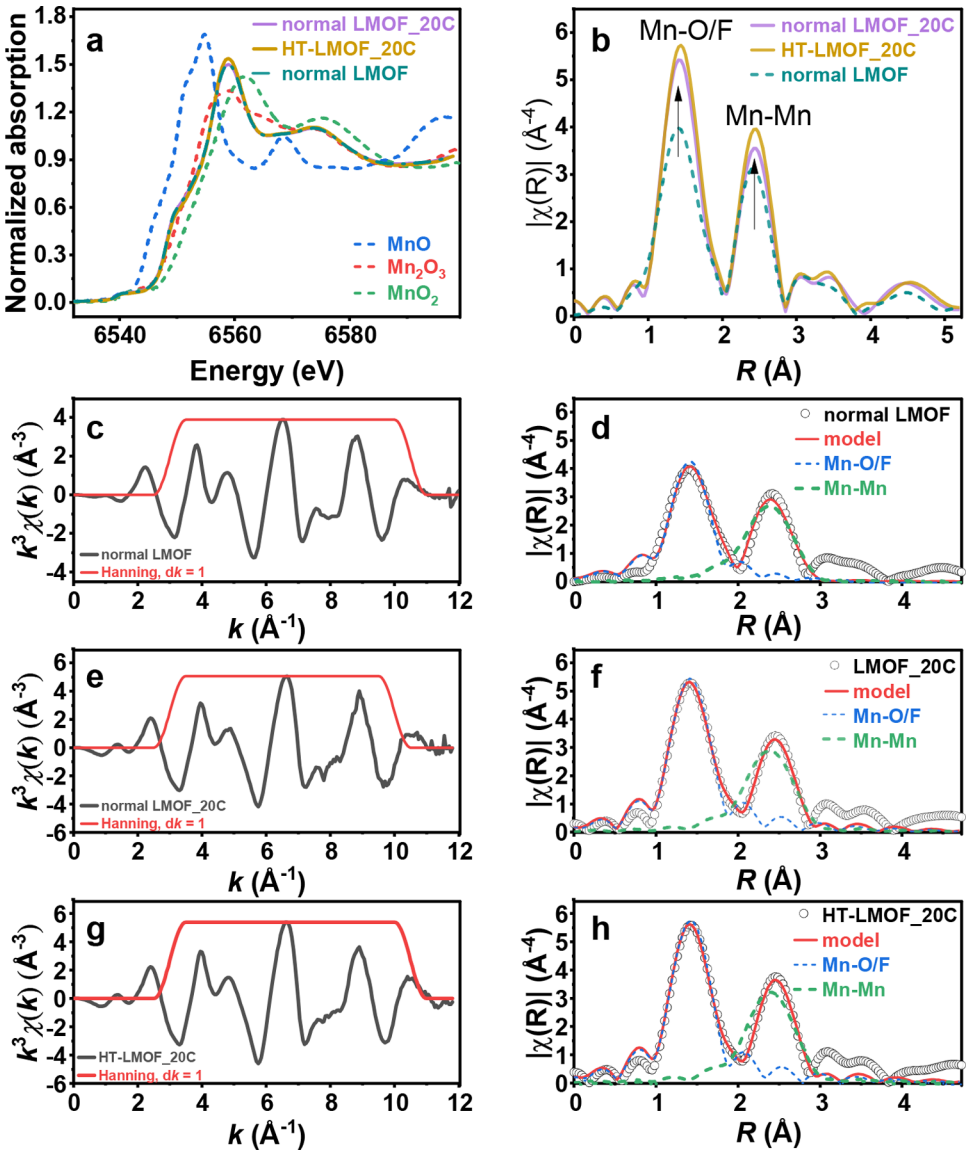

Figure 7. Mn K-edge XAFS spectra of normal LMOF and normal and HT LMOF after 20 cycles in the discharged state measured at ROCK beamline in the SOLEIL synchrotron facility. (a) XANES with standards; (b) comparison of Fourier transform of EXAFS; k^3-weighted $\chi(k)$ with a Hanning window of dk = 1 and shell fitting in the R space for normal LMOF (c and d), normal LMOF_20C (e and f), and HT-LMOF_20C (g and h).

Table 2. Fitting Results from the Mn K-Edge[a]

			Mn−O/F			Mn−Mn			
sample	S02	*E*0 (eV)	*R* (Å)	C. N.	σ^2(Å^2)	*R* (Å)	C. N.	σ^2(Å^2)	*r* factor
normal LMOF	0.98 (fixed)	−7.9 ± 2.4	1.896 ± 0.009	1.7 ± 0.3	0.003 ± 0.002	2.92 ± 0.01	3.8 ± 1.3	0.015 ± 0.003	0.010
normal LMOF_20C		−4.4 ± 1.3	1.890 ± 0.006	2.0 ± 0.2	0.002 ± 0.001	2.90 ± 0.01	3.6 ± 0.8	0.014 ± 0.002	0.004
HT-LMOF_20C		−3.5 ± 1.3	1.895 ± 0.006	2.1 ± 0.2	0.014 ± 0.002	2.91 ± 0.01	3.9 ± 0.8	0.014 ± 0.002	0.004

[a]S02 is fixed to 0.98.

as the determination of capacity retention, rate capability, and cell impedance upon cycling. In addition, the effects of further heat treatment of the materials were investigated. The manganese-based cathode materials $Li_2Mn_{1-x}V_xO_2F$ were successfully synthesized, mainly for comparison of x = 0.5 with x = 0. For x = 0.5, vanadium substitution was achieved while maintaining the DRS structure. In both syntheses, XANES confirmed that the TMs maintained their oxidation state with respect to the precursors.

The results of the electrochemical tests are summarized in Table 3. With respect to the normal samples, LMVOF shows a higher capacity retention after 100 cycles. Here, the heat treatment process leads to an enhanced result in both cases, especially for the LMOF sample. In general, the LMOF samples show a better rate capability, but this property was improved for LMVOF by heat treatment. The impedance growth of the HT-LMVOF electrode was lower than that of the normal LMVOF. However, the impedances of the LMOF

https://doi.org/10.1021/acsmaterialsau.2c00064
ACS Mater. Au XXXX, XXX, XXX−XXX

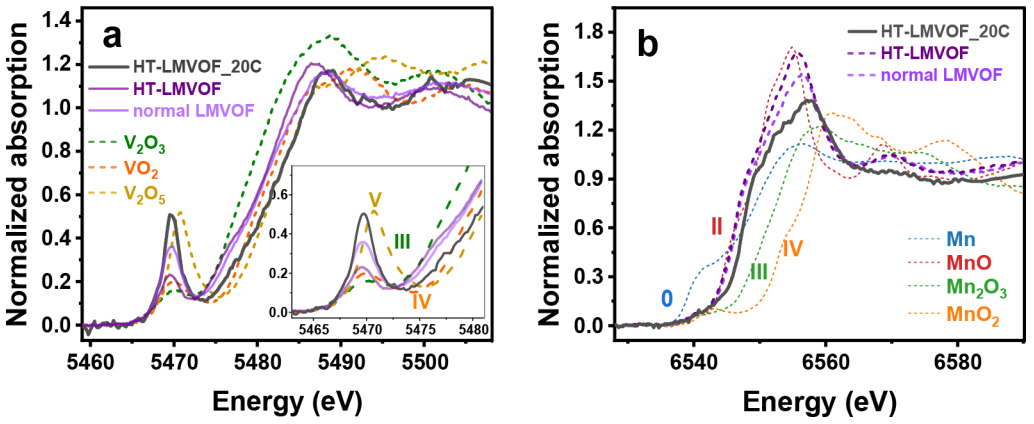

Figure 8. (a) Vanadium and (b) manganese K-edge XANES spectra of the cycled LMVOF_20C electrode in the discharged state.

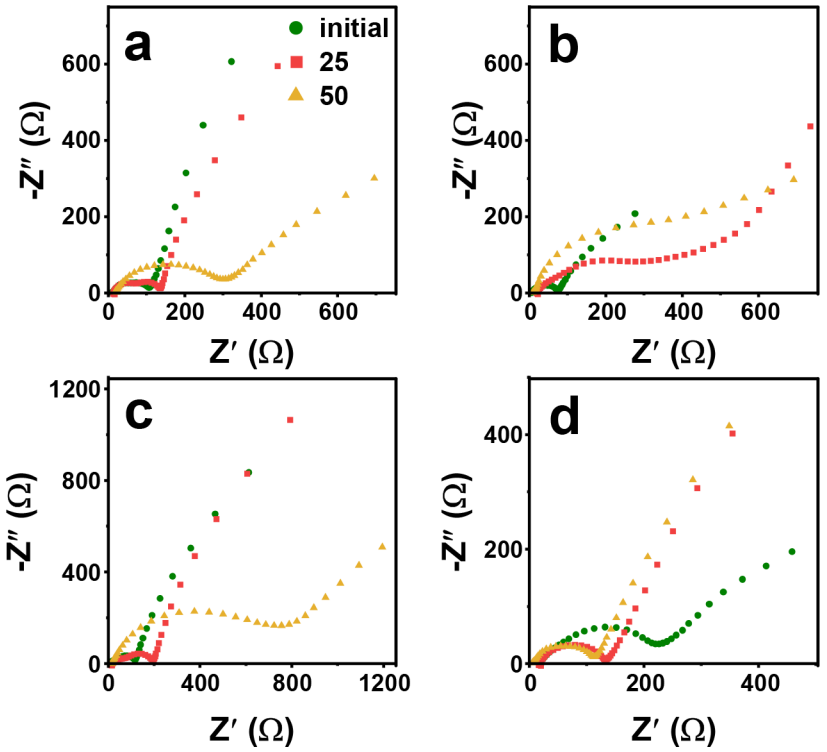

Figure 9. EIS Nyquist plots at the initial state and after the 25th and 50th cycles for (a) normal LMOF, (b) HT-LMOF, (c) normal LMVOF, and (d) HT-LMVOF.

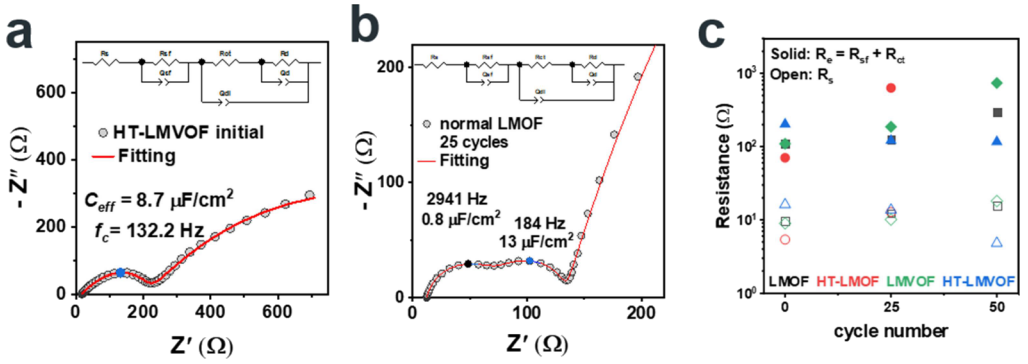

Figure 10. Examples of impedance fitting using the equivalent circuit shown as inset (a,b). C_{eff} denotes the effect of capacitance obtained by $C_{eff} = \frac{1}{2\pi R f_c}$ and f_c denotes the characteristic frequency of the respective semicircle. Evolution of ohmic (open symbols) and total electrode resistances ($R_{sf} + R_{ct}$, solid symbols) (c).

https://doi.org/10.1021/acsmaterialsau.2c00064
ACS Mater. Au XXXX, XXX, XXX−XXX

Table 3. Summary of the Obtained Results of the Electrochemical Cell Tests

		normal sample	HT sample
capacity retention (100 cycles)	LMOF	∼31%	∼81%
	LMVOF	∼44%	∼50%
rate capability		LMOF > LMVOF	improved for LMVOF
EIS	LMOF	no visible effect of heat treatment on impedance	
	LMVOF	positive effect of heat treatment on impedance	

samples did not show drastic changes before and after heat treatment. The substitution of half of the manganese with vanadium did not lead to significant improvements in terms of electrochemical properties compared to the base compound Li_2MnO_2F. However, if we consider LMVOF and Li_2VO_2F (LVOF), which was reported earlier, we can see that LMVOF has a better capacity retention after 50 cycles compared to the initial state (LVOF: 36−37% vs LMVOF: 59%).[10]

Compendiously, heat treatment has a positive effect on the electrochemical performance of both materials, but they still suffer from certain capacity fading. Nevertheless, the study opens up a way for a new consideration of Li-rich DRS as cathode candidates for high energy density LIBs.

EXPERIMENTAL SECTION

Material Synthesis

Two compounds, Li_2MnO_2F (LMOF) and $Li_2Mn_{0.5}V_{0.5}O_2F$ (LMVOF), were prepared in a two-step synthesis by high-energy mechanochemical ball-milling. The as-synthesized samples without further processing are referred to as normal samples. For synthesizing LMOF, in the first step, Li_2O (99.7%, Alfa Aesar) and Mn_2O_3 (99%, Alfa Aesar) were mixed in a stoichiometric ratio under an inert atmosphere. The mixture was filled in a silicon nitride jar (80 mL) with 10 mm balls (ball-to-powder ratio of 13:1) and milled at 600 rpm (Fritsch P6 planetary ball mill) for 20 h (10 min rest after each 30 min milling interval). In the second step, LiF (99.9%, Alfa Aesar) was added under an inert atmosphere in a stoichiometric ratio to the mixture. The powders were then again milled for another 20 h at 600 rpm under the same conditions.

For synthesizing LMVOF, Li_2O (99.7%, Alfa Aesar), MnO (99.99%, Alfa Aesar), and VO_2 (99%, Alfa Aesar) were mixed as precursors also under an inert atmosphere in stoichiometric ratios. A hardened stainless steel jar (80 mL) and balls (10 mm) with a ball-to-powder ratio of 32:1 were used for this synthesis. This mixture and the mixture obtained with the addition of LiF (99.9%, Alfa Aesar) were each milled at a rotation speed of 500 rpm following the same procedure as described above. In addition to the two compounds mentioned above, we also tried to synthesize $Li_2Mn_{0.66}V_{0.33}O_2F$. For this purpose, Li_2O (99.7%, Alfa Aesar), Mn_2O_3 (99%, Alfa Aesar), and V_2O_3 (99.7%, Alfa Aesar) were used as precursors. Two synthesis attempts were made, the conditions of which were analogous to the above syntheses of LMOF and LMVOF.

Heat Treatment

To improve the stability and performance, the synthesized materials were further heat-treated (HT). For the heat treatment, 500 mg of each powder was pressed into pellets. The pellets were then heated three times, respectively, for 5 h up to 300 °C at a constant rate of 80 °C/h under a forming gas atmosphere.

Material Characterization

Powder XRD patterns were recorded using an STOE STADI-P diffractometer (equipped with a DECTRIS MYTHEN 1K strip detector) in the transmission mode with Mo Kα1 radiation (0.70932 Å) in a 2θ range of 10°−50°. All measurements were carried out with an airtight sample holder fitted with an acetate foil window. In order to select a suitable temperature for the heat treatment process, DSC heating runs (TA Instruments, Discovery DSC CFN-50) were performed at a heating rate of 5 °C/min.

The structure and elemental distribution of the sample were investigated by TEM and HAADF−STEM−EDX mapping measurements under a 300 kV operation voltage performed using a double-corrected Thermo Fisher Themis-Z equipped with a Super-X EDX detector. To determine the morphology of the synthesized powders, SEM with in-lens detection at 10 keV was carried out using a ZEISS GEMINI Crossbeam 350 field-emission SEM. Additionally, an EDX analysis was performed. For that, an OXFORD XMAX 50 detector (10 keV) and Aztec software were used.

Transmission XANES was carried out for Mn and V K-edges using the easyXAFS300+ laboratory device (easyXAFS LLC, Renton, WA). An appropriate amount of materials was diluted with cellulose and pressed into pellets, which were later sandwiched by Kapton tapes and mounted onto the sample holder.[27] Transmission XAFS was carried out using an energy step of 0.25 eV for the XANES region and a step of 0.03 $Å^{-1}$ for the postedge region. Multiple scans for each sample were conducted to improve the signal-to-noise ratio. Metal reference foils (Goodfellow or Exafs Materials, Danville, CA) were measured each time before and after measuring the LMOF and LMVOF samples and standards for energy calibration as well as for monitoring the energy drift. More details on the sample preparation and data acquisition are described elsewhere.[7] The absorption spectra were calculated according to the transmission relation $\mu(E) \sim \ln(I_0/I_t)$ using Python-based software (easyXAFS LLC), which was also used for the dead time correction and energy calibration. The reduced data were further processed and analyzed using Larch software.[28]

In addition, synchrotron Mn K-edge XAFS was performed on cycled electrodes (20 cycles, discharge state) at ROCK[29,30] beamline at the SOLEIL synchrotron facility (proposal number 20210779). The storage ring was operated in uniform top-up at 2.75 GeV with a current of 500 mA. ROCK is a beamline with three quick-EXAFS monochromators where the hard X-ray photons come from a superbending magnet (2.81 T). The beam is focused horizontally thanks to a collimating toroidal Ir-coated mirror. The harmonics are rejected by two mirrors tilted at 3.5 mrad using the B4C stripes, and a Si(111) quick-EXAFS monochromator was used. The beam size was 1.2 mm in horizontal and 0.35 mm in vertical at the sample position. The oscillation speed of the monochromator was 2 Hz at the Mn K-edges, which allowed the acquisition of a full XAFS spectrum in 250 ms. The signal was collected in transmission using gas ionization chambers as detectors. These three detectors, connected in series, allowed simultaneous recording of a Mn metal sheet, which was used as a reference to calibrate the energy for each spectrum. The reference standards were prepared by diluting the $Mn^{II}O$, $Mn_2^{III}O_3$, and $Mn^{IV}O_2$ powders with cellulose and pressing into pellets.[7] Electrode tapes of normal LMOF and HT-LMOF were prepared according to the method described below. After cycling (20 cycles), the tapes were washed in dimethyl carbonate and sealed in a small Mylar bag in an Ar-filled glove box using a heat sealer. Standard pellets were wrapped using Kapton tapes. Mn K-edge spectra were extracted and averaged over continuous >1000 scans (elapsed time >500 s and exposure >250 s) with an energy grid of 0.2 eV for the near-edge region and 2 and 1 eV for the pre- and postedge range, respectively. LMOF and HT-LMOF were compared with standards. EXAFS spectra were extracted using the AUTOBK algorithm.[31] A smooth quadratic spline polynomial with R bkg = 1 $Å^{-1}$ in the k range of 0−12 Å was used for background subtraction. The isolated $\chi(k)$ data were k^3-weighted and Fourier-transformed over 3−10.5 $Å^{-1}$ after applying a Hanning window function (dk = 2). A theoretical model was calculated using FEFF8 in xrayLarch.[28,32] The amplitude reduction factor S02 was obtained from fitting the MnO standard and fixed as 0. For the first coordination shell, O and F were not resolved due to the disorder of anions in the DRS system and the limited k range.

https://doi.org/10.1021/acsmaterialsau.2c00064
ACS Mater. Au XXXX, XXX, XXX−XXX

Electrochemical Performance

To determine the electrochemical performance of the synthesized materials, electrodes were prepared using the slurry method. The active materials LMOF or LMVOF and conductive Super P carbon black were premixed in a ratio of 60:30 by ball-milling in a silicon nitride jar (20 mL) under an inert atmosphere for 2 h at 200 rpm (Fritsch P7 premium line). The obtained composites were then sieved with a 230 mesh sieve. Polyvinylidene fluoride was added as a binder to the mixed material in a ratio of 10:90 and dissolved in *N*-methyl-2-pyrrolidone using a Thinky Mixer (ARE-250 Thinky Inc.). The final mixture was tape-cast on a thin layer of an aluminum foil and dried in the oven under dynamic vacuum for 12 h at 120 °C. Electrodes were punched into 12 mm discs, containing around 1 mg of the active material. In addition to the cathode part, the electrochemical cells consisted of 1 M $LiPF_6$ in ethylene/diethyl carbonate (EC/DEC, ratio of 1:1, both from BASF) as the electrolyte, a Whatman glass fiber as the separator, and a Li metal foil as the anode, used as both reference and auxiliary electrodes into electrode Swagelok-type cells. The cell assembly was handled in an argon-filled glove box (O_2/H_2O < 1 ppm). After a rest period of 48 h, galvanostatic charge−discharge cycling with a potential limitation of 1.5−4.3 V at 25 °C was performed at various rates using an Arbin BT2000 battery cycler. CV measurements were carried out in the same voltage range using different scan rates (VMP3 potentiostat, BioLogic). EIS was performed at the discharged state (1.5 V) at 25 °C in a frequency range from 1 MHz to 50 mHz with an AC voltage of 20 mV.

■ ASSOCIATED CONTENT

Supporting Information

The Supporting Information is available free of charge at https://pubs.acs.org/doi/10.1021/acsmaterialsau.2c00064.

> Comparison of the XRD patterns of the different samples before and after heat treatment and according to the attempted compositions, DSC results and SEM images of the samples, CV curves at different scan rates, and EIS upon cycling with a larger view (PDF)

■ AUTHOR INFORMATION

Corresponding Authors

Abdel El Kharbachi − *Helmholtz Institute Ulm (HIU), Ulm 89081, Germany*; orcid.org/0000-0003-4332-1544; Email: kharbachi@kit.edu

Maximilian Fichtner − *Helmholtz Institute Ulm (HIU), Ulm 89081, Germany; Institute of Nanotechnology, Karlsruhe Institute of Technology (KIT), Karlsruhe 76021, Germany*; orcid.org/0000-0002-7127-1823; Email: m.fichtner@kit.edu

Authors

Iris Blumenhofer − *Helmholtz Institute Ulm (HIU), Ulm 89081, Germany*

Yasaman Shirazi Moghadam − *Helmholtz Institute Ulm (HIU), Ulm 89081, Germany*

Yang Hu − *Helmholtz Institute Ulm (HIU), Ulm 89081, Germany*; orcid.org/0000-0001-6864-6498

Kai Wang − *Institute of Nanotechnology, Karlsruhe Institute of Technology (KIT), Karlsruhe 76021, Germany*

Complete contact information is available at: https://pubs.acs.org/10.1021/acsmaterialsau.2c00064

Author Contributions

The manuscript was written through contributions of all authors. All authors have given approval to the final version of the manuscript. I.B. and Y.S.M. contributed equally. CRediT: **Iris Blumenhofer** data curation (equal), formal analysis (equal), investigation (equal), methodology (equal), writing-original draft (equal); **Yasaman Shirazi Moghadam** data curation (equal), formal analysis (equal), investigation (equal), methodology (equal), writing-original draft (equal); **Abdel El Kharbachi** conceptualization (equal), supervision (equal), validation (equal), visualization (equal), writing-review & editing (equal); **Yang Hu** data curation (equal), formal analysis (equal), visualization (equal), writing-review & editing (equal); **Kai Wang** formal analysis (equal), investigation (equal), writing-review & editing (equal); **Maximilian Fichtner** conceptualization (equal), funding acquisition (equal), supervision (equal), writing-review & editing (equal).

Funding

This work was partially funded by the German Research Foundation (DFG) under Project ID 390874152 (POLiS Cluster of Excellence).

Notes

The authors declare no competing financial interest.

■ ACKNOWLEDGMENTS

This work contributes to the research performed at the Center for Electrochemical Energy Storage Ulm-Karlsruhe (CELEST). The synchrotron XAFS was conducted at ROCK beamline of the SOLEIL synchrotron facility (proposal number 20210779) and supported by a public grant overseen by the French National Research Agency (ANR) as part of the "Investissements d'Avenir" program (reference: ANR-10-EQPX-45). The authors thank the Karlsruhe Nano Micro Facility (KNMFi).

■ REFERENCES

(1) Christensen, J.; Albertus, P.; Sanchez-Carrera, R. S.; Lohmann, T.; Kozinsky, B.; Liedtke, R.; Ahmed, J.; Kojic, A. A critical review of Li/air batteries. *J. Electrochem. Soc.* **2011**, *159*, R1.

(2) Huggins, R.*Advanced batteries: materials science aspects*; Springer Science & Business Media, 2008.

(3) Tarascon, J.-M.; Armand, M.Issues and challenges facing rechargeable lithium batteries. In *Materials for sustainable energy: a collection of peer-reviewed research and review articles from Nature Publishing Group*; World Scientific, 2011; pp 171−179.

(4) Kurzweil, P.; Dietlmeier, O. K.*Elektrochemische Speicher*; Springer, 2015.

(5) Armand, M.; Tarascon, J.-M. Building better batteries. *Nature* **2008**, *451*, 652−657.

(6) Fergus, J. W. Recent developments in cathode materials for lithium ion batteries. *J. Power Sources* **2010**, *195*, 939−954.

(7) Shirazi Moghadam, Y.; El Kharbachi, A.; Diemant, T.; Melinte, G.; Hu, Y.; Fichtner, M. Toward Better Stability and Reversibility of the Mn4+/Mn2+ Double Redox Activity in Disordered Rocksalt Oxyfluoride Cathode Materials. *Chem. Mater.* **2021**, *33*, 8235−8247.

(8) Shirazi Moghadam, Y.; Dinda, S.; El Kharbachi, A.; Melinte, G.; Kübel, C.; Fichtner, M. Structural and Electrochemical Insights from the Fluorination of Disordered Mn-Based Rock Salt Cathode Materials. *Chem. Mater.* **2022**, *34*, 2268−2281.

(9) House, R. A.; Jin, L.; Maitra, U.; Tsuruta, K.; Somerville, J. W.; Förstermann, D. P.; Massel, F.; Duda, L.; Roberts, M. R.; Bruce, P. G. Lithium manganese oxyfluoride as a new cathode material exhibiting oxygen redox. *Energy Environ. Sci.* **2018**, *11*, 926−932.

(10) Baur, C.; Kallquist, I.; Chable, J.; Chang, J. H.; Johnsen, R. E.; Ruiz-Zepeda, F.; Ateba Mba, J. M.; Naylor, A. J.; Garcia-Lastra, J. M.; Vegge, T.; et al. Improved cycling stability in high-capacity Li-rich vanadium containing disordered rock salt oxyfluoride cathodes. *J. Mater. Chem. A* **2019**, *7*, 21244−21253.

(11) Lee, J.; Seo, D.-H.; Balasubramanian, M.; Twu, N.; Li, X.; Ceder, G. A new class of high capacity cation-disordered oxides for rechargeable lithium batteries: Li−Ni−Ti−Mo oxides. *Energy Environ. Sci.* **2015**, *8*, 3255−3265.
(12) Urban, A.; Lee, J.; Ceder, G. The configurational space of rocksalt-type oxides for high-capacity lithium battery electrodes. *Adv. Energy Mater.* **2014**, *4*, No. 1400478.
(13) Lee, J.; Urban, A.; Li, X.; Su, D.; Hautier, G.; Ceder, G. Unlocking the potential of cation-disordered oxides for rechargeable lithium batteries. *Science* **2014**, *343*, 519−522.
(14) Abdellahi, A.; Urban, A.; Dacek, S.; Ceder, G. Understanding the effect of cation disorder on the voltage profile of lithium transition-metal oxides. *Chem. Mater.* **2016**, *28*, 5373−5383.
(15) Lee, J. H.; Sa, Y. J.; Kim, T. K.; Moon, H. R.; Joo, S. H. A transformative route to nanoporous manganese oxides of controlled oxidation states with identical textural properties. *J. Mater. Chem. A* **2014**, *2*, 10435−10443.
(16) Chen, R.; Ren, S.; Knapp, M.; Wang, D.; Witter, R.; Fichtner, M.; Hahn, H. Disordered Lithium-Rich Oxyfluoride as a Stable Host for Enhanced Li+ Intercalation Storage. *Adv. Energy Mater.* **2015**, *5*, No. 1401814.
(17) Huggins, R. A. Lithium alloy negative electrodes formed from convertible oxides. *Solid State Ionics* **1998**, *113*, 57−67.
(18) Xu, X.; Pi, L.; Marie, J.-J.; Rees, G. J.; Gong, C.; Pu, S.; House, R. A.; Robertson, A. W.; Bruce, P. G. Li2NiO2F a New Oxyfluoride Disordered Rocksalt Cathode Material. *J. Electrochem. Soc.* **2021**, *168*, No. 080521.
(19) Vetter, J.; Novák, P.; Wagner, M. R.; Veit, C.; Möller, K.-C.; Besenhard, J.; Winter, M.; Wohlfahrt-Mehrens, M.; Vogler, C.; Hammouche, A. Ageing mechanisms in lithium-ion batteries. *J. Power Sources* **2005**, *147*, 269−281.
(20) Bhandari, A.; Bhattacharya, J. Manganese dissolution from spinel cathode: few unanswered questions. *J. Electrochem. Soc.* **2016**, *164*, A106.
(21) Zhan, C.; Lu, J.; Jeremy Kropf, A.; Wu, T.; Jansen, A. N.; Sun, Y.-K.; Qiu, X.; Amine, K. Mn (II) Deposition on Anodes and Its Effects on Capacity Fade in Spinel Lithium Manganate-Carbon Systems. *Nat. Commun.* **2013**, *4*, 2437.
(22) Kumai, K.; Miyashiro, H.; Kobayashi, Y.; Takei, K.; Ishikawa, R. Gas generation mechanism due to electrolyte decomposition in commercial lithium-ion cell. *J. Power Sources* **1999**, *81*, 715−719.
(23) Lee, J.; Kitchaev, D. A.; Kwon, D.-H.; Lee, C.-W.; Papp, J. K.; Liu, Y.-S.; Lun, Z.; Clement, R. J.; Shi, T.; McCloskey, B. D. Reversible Mn2+/Mn4+ double redox in lithium-excess cathode materials. *Nature* **2018**, *556*, 185−190.
(24) Kitchaev, D. A.; Lun, Z.; Richards, W. D.; Ji, H.; Clément, R. J.; Balasubramanian, M.; Kwon, D.-H.; Dai, K.; Papp, J. K.; Lei, T.; McCloskey, B. D.; Yang, W.; Lee, J.; Ceder, G. Design principles for high transition metal capacity in disordered rocksalt Li-ion cathodes. *Energy Environ. Sci.* **2018**, *11*, 2159−2171.
(25) Kim, T.; Choi, W.; Shin, H.-C.; Choi, J.-Y.; Kim, J. M.; Park, M.-S.; Yoon, W.-S. Applications of voltammetry in lithium ion battery research. *J. Electrochem. Sci. Technol.* **2020**, *11*, 14−25.
(26) Tröltzsch, U.; Kanoun, O.; Tränkler, H.-R. Characterizing aging effects of lithium ion batteries by impedance spectroscopy. *Electrochim. Acta* **2006**, *51*, 1664−1672.
(27) Ravel, B.; Newville, M. ATHENA, ARTEMIS, HEPHAESTUS: data analysis for X-ray absorption spectroscopy using IFEFFIT. *J. Synchrotron Radiat.* **2005**, *12*, 537−541.
(28) Newville, M. In Larch: an analysis package for XAFS and related spectroscopies. *J. Phys. Conf. Ser.* **2013**, No. 012007.
(29) La Fontaine, C.; Belin, S.; Barthe, L.; Roudenko, O.; Briois, V. ROCK: A Beamline Tailored for Catalysis and Energy-Related Materials from ms Time Resolution to μm Spatial Resolution. *Synchrotron Radiat. News* **2020**, *33*, 20−25.
(30) Briois, V.; La Fontaine, C.; Belin, S.; Barthe, L.; Moreno, T.; Pinty, V.; Carcy, A.; Girardot, R.; Fonda, E. ROCK: the new Quick-EXAFS beamline at SOLEIL. *J. Phys. Conf. Ser.* **2016**, *712*, No. 012149.
(31) Newville, M.; Līviņš, P.; Yacoby, S. Y.; Rehr, J.; Stern, E. Near-edge x-ray-absorption fine structure of Pb: A comparison of theory and experiment. *Phys. Rev. B* **1993**, *47*, 14126.
(32) Newville, M. EXAFS analysis using FEFF and FEFFIT. *J. Synchrotron Radiat.* **2001**, *8*, 96−100.

Recommended by ACS

Unraveling the Nature and Role of Layered Cation Ordering in Cation-Disordered Rock-Salt Cathodes
You Wang, Dongchang Chen, *et al.*
OCTOBER 18, 2022
JOURNAL OF THE AMERICAN CHEMICAL SOCIETY
READ

Understanding the Fluorination of Disordered Rocksalt Cathodes through Rational Exploration of Synthesis Pathways
Nathan J. Szymanski, Gerbrand Ceder, *et al.*
JULY 18, 2022
CHEMISTRY OF MATERIALS
READ

Na-Rich Disordered Rock Salt Oxyfluoride Cathode Materials for Sodium Ion Batteries
Yasaman Shirazi Moghadam, Maximilian Fichtner, *et al.*
DECEMBER 08, 2022
ACS MATERIALS LETTERS
READ

Structural and Electrochemical Insights from the Fluorination of Disordered Mn-Based Rock Salt Cathode Materials
Yasaman Shirazi Moghadam, Maximilian Fichtner, *et al.*
FEBRUARY 17, 2022
CHEMISTRY OF MATERIALS
READ

Get More Suggestions >

https://doi.org/10.1021/acsmaterialsau.2c00064
ACS Mater. Au XXXX, XXX, XXX−XXX